Acta Cryst. (1983). A**39**, 838–847

High-Resolution Electron Microscopy of Molecular Crystals. II. Image Simulation

BY M. A. O'KEEFE

High Resolution Electron Microscope, University of Cambridge, Free School Lane, Cambridge CB2 3RQ, England

J. R. FRYER

Chemistry Department, University of Glasgow, Glasgow G12 8QQ, Scotland

AND DAVID J. SMITH

High Resolution Electron Microscope, University of Cambridge, Free School Lane, Cambridge CB2 3RQ, England

(*Received* 15 *February* 1983; *accepted* 22 *April* 1983)

Abstract

Computer-simulated electron-microscope images have been produced for several different aromatic hydrocarbons, as well as the organometallic compound chlorinated copper phthalocyanine. Weak-phase-object images are compared with full multislice imaging calculations that include the resolution-limiting effects of limited spatial and temporal coherence; the comparisons indicate a considerable range of focus and thickness where intuitive image interpretation is possible. This favourable situation arises directly from the low atomic numbers of the atoms comprising the molecules and the almost monotonic fall-off with scattering angle of those structure factors within the resolution limit of the microscope. The occurrence and nature of both first- and second-order resolution-limiting effects on typical 100 and 500 kV images is also discussed.

1. Introduction

It is widely recognized that the interpretation of high-resolution electron micrographs of complex structures is greatly facilitated by comparison with computer-simulated images. This is particularly true in the case of beam-sensitive materials when micrographs are frequently obtained under non-optimum conditions. For example, minimum exposure techniques can result in images recorded at variable values of focus or specimen tilt and thickness may not be ideal. Such images generally require careful matching with simulation for reliable interpretation. Examples of beam-sensitive materials requiring image simulations for the interpretation of experimental images include some minerals (see *e.g.* Veblen & Buseck, 1980) and the molecular crystal chlorinated copper phthalocyanine (Uyeda & Ishizuka, 1974); simulations have also been useful (O'Keefe, Fryer & Smith, 1982) in establishing the resolution obtained experimentally in observations of the beam-sensitive aromatic hydrocarbon quaterrylene (Fryer & Smith, 1982).

The molecular and crystal structures of the small organic molecules considered in the present work have been determined previously by X-ray techniques. Thus, reconstruction of their structures from amplitudes and phases derived from the micrographs – such as has been applied to proteins (Unwin & Henderson, 1975) – is not our objective. Rather, it is to establish the variations in image appearance with changes of the microscope and specimen parameters, such as focus and thickness, and thereby to determine the extent to which experimental micrographs can be interpreted in terms of local changes in crystal structure. In comparison with the local structure revealed by electron microscopy, X-ray methods provide little or no information about the molecular configurations at grain boundaries, defects and other sites of discontinuity.

Several characteristics of molecular crystals are of relevance here. They form polymorphs with very little differences of energy between the various forms: for example, unique polymorphs of metal-free phthalocyanine can be formed on KCl (Fryer, 1979), and of copper phthalocyanine on graphite (Saijo, Kobayashi & Uyeda, 1977), simply due to the influence of the substrate. Nevertheless, small changes in the structure of non-aromatic unsaturated molecules can affect their ability to undergo photochemical reactions (Schmidt, 1971). Moreover, crystal degradation under electron bombardment or chemical attack is not always a homogeneous process and a knowledge of the local

0108-7673/83/060838-10$01.50

structure is essential if such behaviour is to be understood. For example, the damage caused by the electron beam has been shown in some materials to commence at single molecular sites (Murata, Fryer & Baird, 1977) and, in some materials, crystalline degradation products remain in the damaged area (Fryer, Camps & Smith, 1982). Yet, electron-beam damage need not limit the application of high-resolution electron microscopy to these materials (for a short review, see Fryer & Smith, 1982). Furthermore, molecular crystals also provide a means of modelling crystal faults on a larger than atomic scale. Dislocations in molecular crystals have core dimensions an order of magnitude larger than those present in metals or alloys, simply because the centres of the units (molecules) making up the crystals are ten to twenty ångstroms apart, rather than the one to two ångstroms of the units (atoms) in a metal.

In all these situations, it is important to be able to recognize the molecular position and orientation in experimental images. Thus, in this work, we have considered the imaging of arrays of planar molecules of varying shapes and sizes. The appearance of these images varies with changes in microscope resolution, objective-lens defocus and crystal thickness and orientation. The simulations reveal these changes and can be used to delineate those domains of experimental conditions within which the molecules may be unmistakably recognized.

2. Structures

The crystal data for a range of aromatic hydrocarbons were used for the simulation of images under a variety of experimental conditions. Initial computations were carried out for quaterrylene, $C_{40}H_{20}$, since experimental images had already been obtained (Smith & Fryer, 1981). Unfortunately, while the quaterrylene molecule is essentially planar, it forms molecular crystals (Kerr, Ashmore & Speakman, 1975) with no crystallographic axis whereon molecular superposition occurs (Fig. 1*a*). Subsequent calculations were extended to three other aromatic hydrocarbons (covering a range of molecular weights) which form crystals having molecular superposition. In order of increasing size these are coronene, $C_{24}H_{12}$ (Robertson & White, 1945) (Fig. 1*b*), ovalene, $C_{32}H_{14}$ (Donaldson & Robertson, 1954) (Fig. 1*c*), and hexabenzocoronene, $C_{42}H_{21}$ (Robertson & Trotter, 1961) (Fig. 1*d*). These three molecules crystallize in space group $P21/a$ with superposition down the b axis, but with the molecular plane tilted so that the molecule normal is inclined to this axis. The angle is relatively large (44, 43 and 47° for coronene, ovalene and hexabenzocoronene, respectively) so that the aromatic rings appear markedly non-regular in b-axis projection. As these molecules are each formed from the same subunit (the 'benzene' ring), with similar inclination to the [010] (superposition) direction, major spacings in the projected structures are similar, producing strong structure factors at similar spatial frequencies: two of the strongest occur near $(2{\cdot}1\ \text{Å})^{-1}$ and $(1{\cdot}6\ \text{Å})^{-1}$, corresponding to the major and minor diameters of the projected aromatic rings. Finally, simulations were carried out for the heterocyclic organometallic chlorinated copper phthalocyanine, $C_{32}Cl_{16}CuN_8$ (Fig. 1*e*). In comparison with the aromatic hydrocarbons, the presence of different ring types in this molecule produces a more complex frequency spectrum, and hence greater variations in the images are produced; the images were computed from the atom positions given by Kirkland (1982).

3. Computation

Images were simulated with the *SHRLI* package (O'Keefe & Buseck, 1979) of Fortran programs installed on a System Engineering Labs 32/27 minicomputer, using the atomic scattering factors listed in *International Tables for X-ray Crystallography* (1974), Table 2.2*B*.

A typical simulation (*e.g.* for hexabenzocoronene) commenced with the computation of 8587 structure factors in the $h0l$ zone out to 5 Å^{-1} (corresponding to $h = \pm 92$ and $l = \pm 63$). These structure factors were used to produce an atlas of all weak-phase-object (WPO)

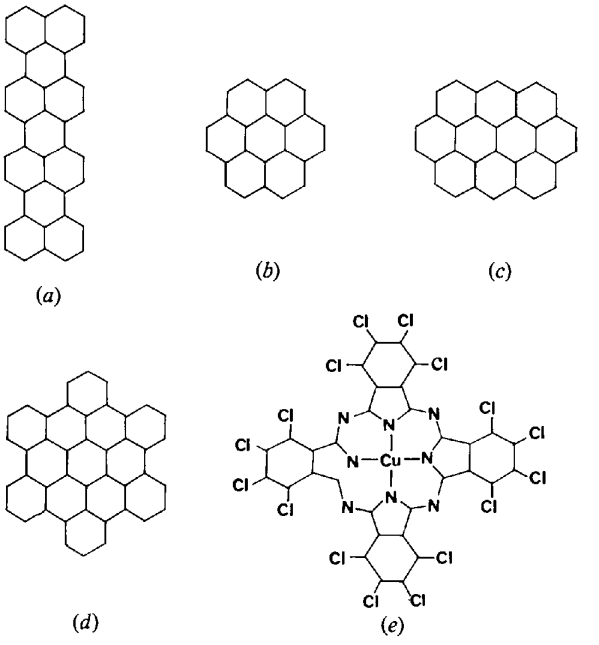

Fig. 1. Carbon skeleton diagrams showing individual molecules of polynuclear aromatic hydrocarbon and phthalocyanine: (*a*) quaterrylene; (*b*) coronene; (*c*) ovalene; (*d*) hexabenzocoronene and (*e*) copper hexadecachlorophthalocyanine.

images (O'Keefe & Pitt, 1980; Smith & O'Keefe, 1983) in the resolution range from 8·7 Å (corresponding to five contributing reflections) to 1 Å (349 reflections). To incorporate the effects of dynamical diffraction and microscope aberrations, further calculations used full multislice programs (Goodman & Moodie, 1974). Dynamical scattering was calculated in thickness steps of 5·11 Å, and the results stored after every five slices increment in thickness, up to 100 slices, for later imaging calculations. The structure factors (and phase-grating coefficients) were deliberately extended to twice the scattering angle of the outermost diffracted beams incorporated in the multislice calculation in order to include all relevant dynamical interactions correctly (Self, O'Keefe, Buseck & Spargo, 1983). 2149 reflections (out to 2·5 $Å^{-1}$) were carried through the dynamical scattering calculations; their normalized intensity sum was 0·9988 after 100 slices.

Images were mainly calculated at an accelerating voltage of 500 kV with microscope parameters of spherical aberration coefficient, C_s = 3·5 mm, convergence semi-angle, α_i = 0·3 mrad, and focal-spread half-width, Δ = 250 Å. (These values correspond to those formerly applicable to the Cambridge 600 kV high-resolution electron microscope – see Smith, Camps, Freeman, Hill, Nixon & Smith, 1983). The objective aperture cutoff was chosen to correspond to 0·7 $Å^{-1}$, since there are no contributions to the image (either directly or *via* second-order interferences) from beams beyond the cutoffs of 0·45 and 0·65 $Å^{-1}$ imposed by the chosen values of Δ and α_i. Images calculated at 100 kV had C_s = 0·7 mm, α_i = 1·0 mrad and Δ = 100 Å. All images were stored on magnetic tape, and later written directly onto photographic film using an Optronics Photowrite System P-1500 with 256 grey levels and 256 pixels of 50 μm size across each image.

4. Results

4.1. *Weak-phase-object (projected potential) images*

In principle, WPO images are produced from any material which can be made sufficiently thin. In practice, certain crystals cannot satisfy this criterion. The critical thickness is an inverse function of the range of the crystal potential (*i.e.* maximum minus minimum) projected in the direction of the incident electron beam. It is also a function of the electron energy and, to a lesser extent, the image resolution (Jap & Glaeser, 1980). For materials of high atomic number viewed along principal axes, the projected potential maxima are high, so that the critical thickness is low (of the order of a unit cell for gold viewed at 100 keV). However, in the case of the low-Z molecules under consideration here, comparison with images from multislice calculations show a critical thickness of around 250 Å for a resolution of about 3·5 Å at an electron energy of 500 keV.

The weak-phase-object image is useful since it is independent of all microscope parameters except for the resolution set by the crossover frequency of the linear-image contrast transfer function at Scherzer focus. A resolution series of WPO images is quickly and easily calculated from structure amplitudes to form an atlas containing all possible WPO images of the structure in the selected orientation (O'Keefe & Pitt, 1980).*

Because it is a linear function of the projection of the crystal potential in the incident-beam direction, the WPO image is (at least quite often) that image which appears most like our intuitive expectation for an image of the structure. However, these WPO or projected potential images (or 'structure images') are a sensitive function of their resolution (O'Keefe, 1973; O'Keefe, Buseck & Iijima, 1978) and may even appear misleading at certain material-specific values of resolution (O'Keefe & Buseck, 1979).

Some such irregularities occur in the resolution series of WPO images of the present materials. Fig. 2 shows the (projected) model structures and WPO images (selected from complete atlases) at resolutions from 7 to 1 Å for (*a*) quaterrylene, (*b*) coronene, ovalene and hexabenzocoronene, and (*c*) copper hexadecachlorophthalocyanine. The superposed aromatic rings are clearly seen in the three models of Fig. 2(*b*), but quaterrylene in 010 orientation is much less clear due to the projection of columns of molecules aligned at both 81 and 9° to the column axis: the model (*a*) shows two parallel rows of eight high-density regions per (primitive) projected unit cell. At 7 Å resolution the unit appears as a black bar, with thickened ends, lying vertically on the page. At 6·3 Å resolution this bar shows three thickened regions that become four at 4·7 Å. The four black spots split along a vertical axis to become eight at 3·8 Å resolution, but the unit formed by the group of eight spots no longer lies vertically on the page. As resolution is increased the eight-spot unit becomes vertical once more; however, at this one particular resolution, a misleading structure image is produced.

For the three superposable aromatic hydrocarbons (*b*), the WPO series show that the molecular positions are unmistakable at 6 to 8 Å, and that good resolution of the molecular shapes is obtained at about 4 Å resolution. However, detail inside the molecule is untrustworthy for resolutions much worse than 2 Å. Near this value of resolution, differences between the orientations of the molecules produced visible effects; at 2 Å resolution the individual rings can be counted in

* Atlases for the structures considered in this present paper are available from the authors.

images of coronene and ovalene, but hexabenzocoronene shows only strong fringes across the molecules. Since the molecular tilt axis in hexabenzocoronene runs across the largest diameter of the aromatic rings, tilting about this axis produces a higher major-to-minor axis ratio than tilting about the tilt axis running across the smallest diameters, as occurs in coronene and ovalene. In hexabenzocoronene the rings can be counted confidently at 1·6 Å resolution.

In WPO images of copper hexadecachlorophthalocyanine (Fig. 2*c*), the outline of the molecular shape is visible at 7 Å resolution. Black spots are seen at the Cu and Cl atom positions at 2½ Å resolution, the six-membered N–C–N–Cu–N–C rings appear at 2 Å,

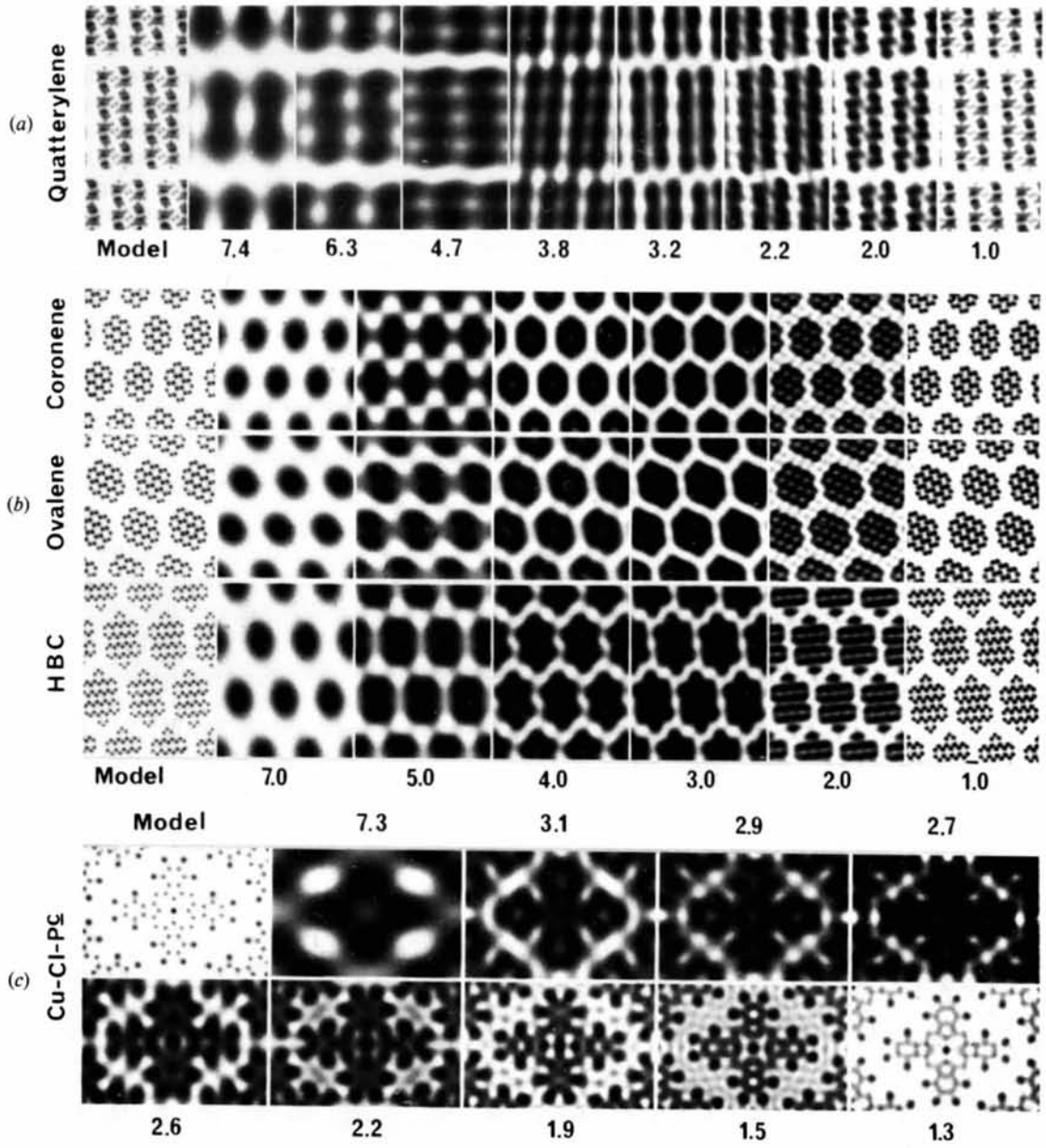

Fig. 2. Projected structure of several molecular crystals with corresponding weak-phase-object images for a range of resolution (marked in Å). (*a*) Quaterrylene in [110] orientation. The model shows the superposed carbon atoms of four molecules forming two parallel rows of eight black spots per (primitive) unit cell. The WPO images range from 7·4 to 1·0 Å resolution: each covers an area of 17 by 38 Å and shows 2·3 × 2 unit cells. (*b*) Coronene, ovalene and hexabenzocoronene (top to bottom) in [010] orientation. The models show superposed tilted molecules containing seven, ten and thirteen aromatic rings, respectively. The WPO images range from 7 down to 1 Å resolution: each is 27 Å across. (*c*) Copper hexadecachlorophthalocyanine in [010] orientation. Molecules superpose and the three ring types are visible in the model. The WPO images from 7·3 to 1·3 Å resolution; each covers an area of 26 × 17·6 Å.

and the five-membered isoindole (C–C–N–C–C) rings are clearly visible by 1·7 Å. Individual atoms are resolved at 1 Å resolution. An interesting artefact is that although the isoindole rings seem to be visible in the horizontal arms at 2·6 Å resolution they are not seen in the vertical arms, and in fact disappear again when resolution is improved to 2·2 Å.

4.2. *Focal series*

The WPO image is a good approximation to the actual image obtained from a thin crystal imaged close to the optimum Scherzer defocus. However, some differences occur due to the 'softness' of the effective aperture imposed by the acting resolution-limiting aberration [probably incident-beam convergence in the 100 keV electron microscope or chromatic aberration in electron microscopes operating at voltages of 500 kV and higher (Smith, 1980)]. In addition, the shape of the contrast transfer function (CTF) is never the ideal one assumed in WPO theory, especially when some transfer occurs beyond the Scherzer limit. Full dynamical (multislice) images incorporate these effects and produce a better match to experimental micrographs, particularly where the crystal thickness approaches, or even exceeds, the critical WPO value. Since experimental micrographs of beam-sensitive specimens are usually obtained at defocus values away from the optimum, images were simulated (for an accelerating voltage of 500 kV) over a range of defocus values for each of the molecular crystals considered. Microscope parameters were set to those values specified above (see § 3) and the defocus range was typically from 1000 Å (overfocus) to −4000 Å (underfocus) in 100 Å steps. Fig. 3 shows how the ovalene image changes over a focus range of 2600 Å for crystal thicknesses of (*a*) 24 Å (five unit cells) and (*b*) 94 Å (20 unit cells).

As might be expected, both focal series indicate that the basic WPO-like image showing the molecular shape (the structure image) persists over an extended defocus range around Scherzer focus (approximately −400 through −1000 Å). Furthermore, comparison of (*a*) and (*b*) reveals that the structure image is not very sensitive to the change of thickness from 24 to 94 Å although images at larger values of underfocus are. A good idea of the resolution in the structure image may be obtained by comparison with the WPO series of Fig. 2. Such a comparison reveals that the structure-image resolution is close to 3 Å at −700 Å defocus and degrades slightly (the molecular shapes becoming more rounded) as the defocus is increased to −1000 Å. In the focal series of the thinner material it is noticeable that the resolution (in terms of detail that can be related to the structure) continues its progressive degradation as

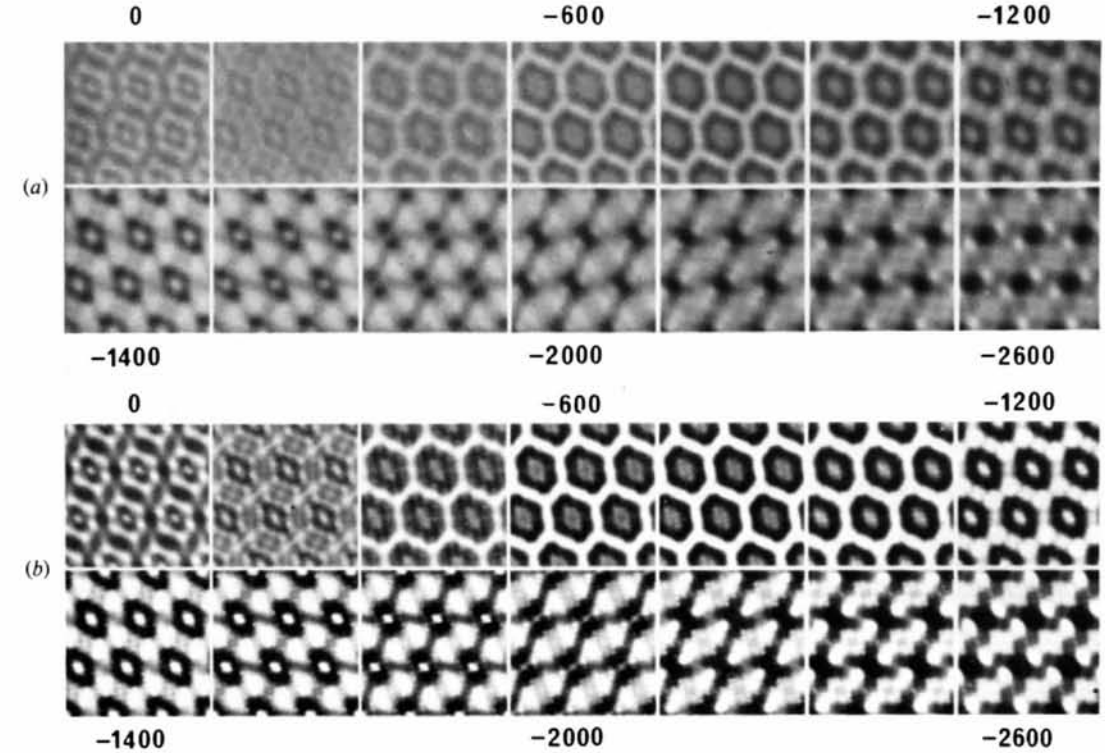

Fig. 3. Focal series of simulated images for ovalene ranging from zero (Gaussian) focus to 2600 Å underfocus for crystals of thickness (*a*) 24 Å and (*b*) 94 Å. Images were computed for 500 kV and C_s of 3·5 mm giving a Scherzer defocus of −700 Å. Resolution limited by focal spread, Δ, of half-width 250 Å and incident-beam convergence, α_i, of semiangle 0·3 mrad.

underfocus is increased to −2400 Å, where only a single black spot remains to indicate the position of each molecule. In fact, the same is true of the linear-image contribution to the thicker focal series, where an increased amount of non-linear high-frequency non-structural detail tends to obscure the worsening resolution.

The progressive degradation of resolution with increasing underfocus may be explained by examining the size of the objective-lens phase change, modulated by the linear envelope functions due to chromatic aberration and incident-beam convergence. In general, the use of such a damped 'contrast transfer function' is an overly simplistic method of examining an electron microscope image. However, 24 Å of ovalene is a good approximation to a weak phase object and thus its image intensity spectrum may be safely considered to be related linearly to its amplitude spectrum by ignoring all but 000–*hkl* interferences (that this approximation is beginning to break down at 94 Å thickness can be seen by the much higher proportion of non-linear or second-order detail at high values of underfocus in Fig. 3 – at lower values of underfocus, particularly near Scherzer focus, the strong linear-image contrast masks the non-linear contribution, and 94 Å may be regarded as lying below the critical WPO crystal thickness).

Plots of the corresponding linear-image CTF's (Fig. 4) demonstrate how spatial frequencies are transferred to the image intensity spectrum and thus how the image is formed. At −400 Å defocus, spatial frequencies to 0·33 Å^{-1} are transferred into the image, producing an image of 3 Å resolution with low contrast (Fig. 3*a* at −400 Å) since the maximum magnitude of the CTF is only 0·4. At −600 Å defocus the maximum magnitude is 0·7 and the cutoff frequency is 0·42 Å^{-1}, so that image contrast and resolution improve (Fig. 3*a* at −600 Å). The improvement continues for −800 Å defocus, but at −1000 Å the cutoff frequency drops to 0·35 Å^{-1} (close to that at −400 Å defocus) and this loss of resolution is reflected in the image (Fig. 3*a* at −1000 Å). As underfocus is increased past −1000 Å, contrast at the lower frequencies remains high, but the cutoff frequency drops (to 0·27, 0·22 and 0·17 Å^{-1} at −1200, −1600 and −2400 Å, respectively), producing lower-resolution images. As the defocus is extended past −1200 Å, the higher spatial frequencies will be phase-reversed and thus contribute to the image with inverse contrast. However, in these low-*Z* materials (with high Debye–Waller factors), the high-frequency components have low amplitudes so that reversal results in their being swamped by the stronger low-frequency contributions. This behaviour is in contrast to that obtained with many inorganic materials (*e.g.* the niobium oxides described by O'Keefe, 1973) where phase reversal of strong high-frequency contributions leads to overall reversal of image contrast.

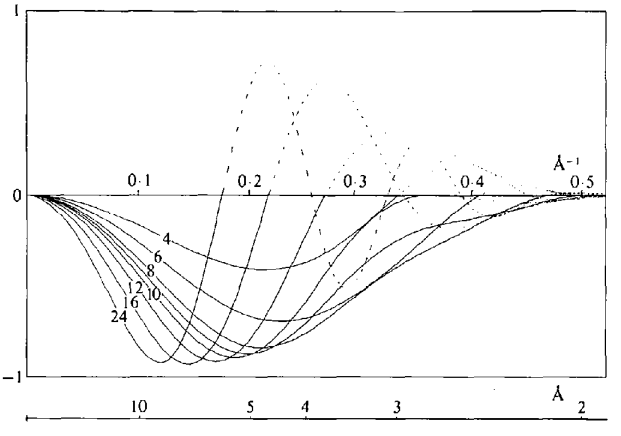

Fig. 4. Linear image CTFs at 500 keV for C_s, Δ and α_1 as in Fig. 3 and defocus values from −400 (curve 4) to −2400 Å (curve 24). At small defocus values (*e.g.* −400 Å), low-contrast low-resolution images are produced owing to the low amplitude and crossover frequency of the CTF. Increasing underfocus initially produces higher values of contrast and resolution but eventually the crossover frequency drops again decreasing the resolution although the contrast remains high.

4.3. *Effect of crystal thickness*

The ovalene images shown in Fig. 3 were selected from a two-dimensional 'map' of simulated images computed over a range of crystal thickness and objective-lens defocus. Such maps were computed for each of the five materials considered here, and are available on request. A portion of one such map (for hexabenzocoronene) is shown in Fig. 5 and can be used to demonstrate the behaviour of the image with increasing crystal thickness for values of defocus close to the Scherzer optimum.

The increase in image contrast near the Scherzer focus is visible in the first column of Fig. 5; this agrees with similar increases found for images of complex oxides (Lynch, Moodie & O'Keefe, 1975). Similarly, with both types of crystal, increasing thickness increases the image contrast and narrows the range of defocus over which the structure image occurs. However, unlike the complex oxide case, in hexabenzocoronene there is *no* marked shift towards zero focus in the position of maximum contrast as crystal thickness increases. The almost monotonic fall-off in structure amplitude with scattering angle is responsible for this docile behaviour just as occurs in Fig. 3 where increasing underfocus produces merely degradation of resolution rather than contrast reversals. Nevertheless, although the best structure image remains near Scherzer defocus (−800 Å in Fig. 5), it occurs over the range −500 to −1000 Å for a 50 Å thick crystal, over −600 to −900 Å at 150 Å thickness, and over only −700 to −900 Å for a thickness of 250 Å. Above this thickness,

the increasing proportion of high-frequency second-order contributions to the intensity spectrum produces molecular images with detail finer than the linear resolution imposed by the objective aperture.

It is tempting to try to relate this fine detail to the molecular structure – *e.g.* the image at −700 Å defocus from a crystal of 360 Å thickness appears to show a black benzene ring with a central white spot at the top and bottom of each molecule, with four more at the 'shoulders' of the molecular outline, and two (weaker) ones in the body of the molecule. A glance at the model in Fig. 2 reveals that each molecule consists of rows of rings; in order (from the top) these rows contain 1,4,3,4, and 1 rings. Thus, in the image at −700 Å from 360 Å, those white spots that occur at top and bottom and at the shoulders are close to ring centres, but the internal structure of the molecule is far from being revealed. The failure of second-order interferences to produce true molecular detail in images from thicker crystals is due to their (relatively) complex structure compared with some simple systems where second-order interferences produce thick-crystal images that mimic structure images of twice the linear-image resolution, as, for example, in the case of β-SiC in [110] orientation (Smith & O'Keefe, 1983).

More complicated systems (*i.e.* ones containing more spatial frequencies) are even less likely to produce fine *structural* detail in images from thicker crystals. Fig. 6(*a*) shows a thickness series of 500 kV images for chlorinated copper phthalocyanine near Scherzer defocus. Comparison with Fig. 2 shows that the thin-crystal (40 Å) image is a structure image of between 2·7 and 2·2 Å resolution showing black spots at the central Cu atom with four black spots in each

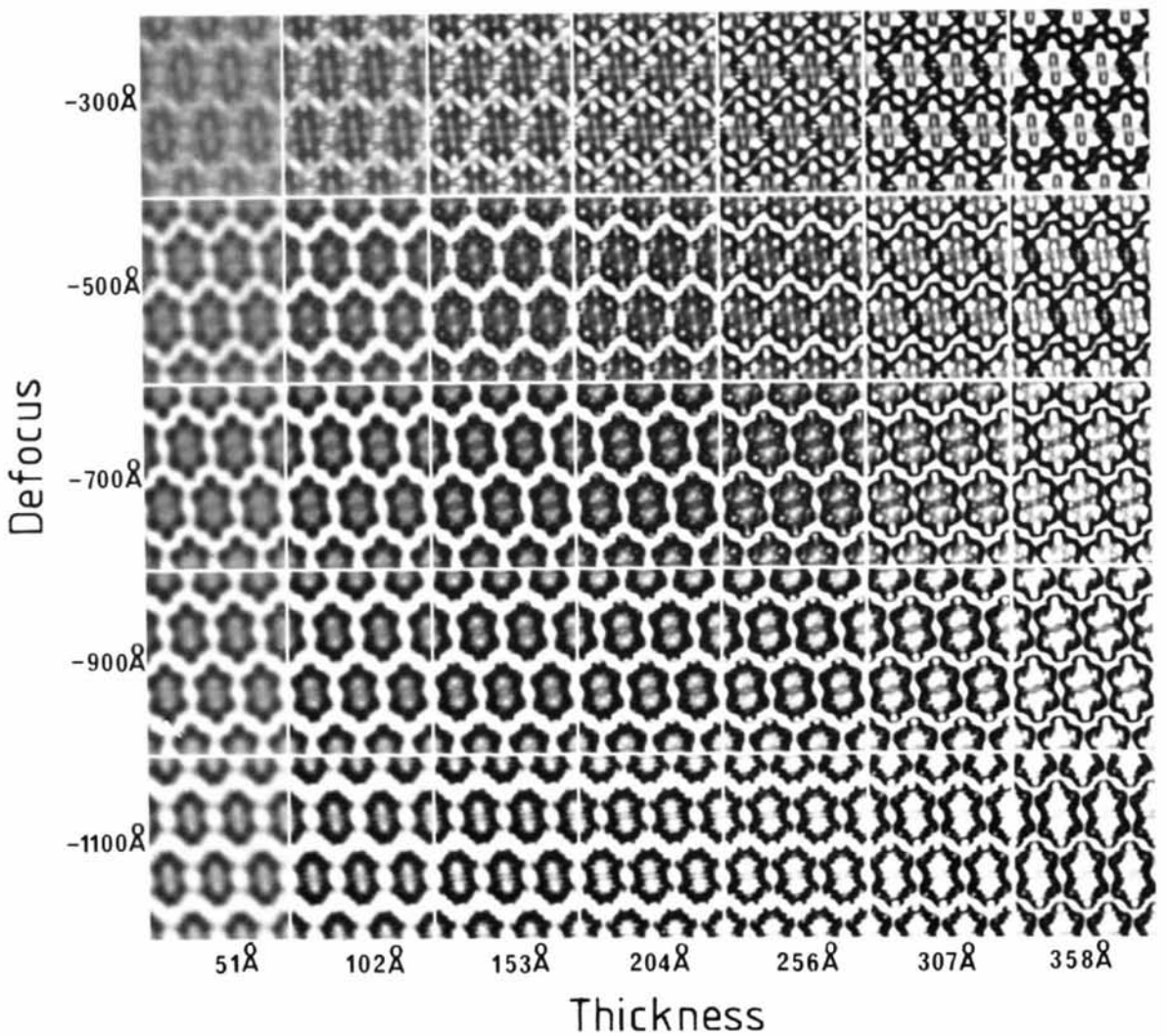

Fig. 5. Simulated images of hexabenzocoronene with increasing crystal thickness up to 360 Å for defocus values around the Scherzer value of −700 Å. Other image parameters are as for Fig. 3.

arm of the molecule corresponding to an unresolved Cl–C atom pair. As thickness increases, an increasing proportion of second-order contributions introduces high-frequency detail, in particular producing central white dots in the black spots corresponding to areas of heavier (Cu and CCl) atomic density in the structure image. Whereas the phases of the linear (first-order) contributions to a structure image are chosen to be negative (by selecting Scherzer focus), strong second-order contributions (in particular those from interferences between **g** and minus **g** reflections) generally have positive phase and produce white peaks at atom positions; these white peaks are sharper (coming from the high-frequency region of the intensity spectrum) than the linear black peaks, and produce the characteristic 'black donut with white hole' image in thicker structure images. Pirouz (1981) has shown that inclusion of the second-order terms is equivalent to adding a term proportional to the square of the projected crystal potential, and yet another proportional to the projected charge density, to the thin-crystal projected potential (WPO) image; a negative-going (black) peak in the WPO image (due to an atom or group of unresolved atoms) is thus squared to add a sharper positive-going (white) peak into the total (linear plus non-linear) image.

Notwithstanding the addition of white dots producing 'donut' atoms, the image at −700 Å defocus in Fig. 6(*a*) is recognizably a structure image of phthalocyanine up to a crystal thickness of 200 Å. However, this critical crystal thickness is lower at lower accelerating voltages. Fig. 6(*b*) shows a thickness series of images calculated for a typical high-resolution electron microscope with an accelerating voltage of 100 kV and covering the same thickness range as in (*a*). The thin-crystal image at Scherzer defocus (−580 Å) is a structure image of between 3·1 and 2·7 Å resolution (at 3·1 and 2·7 Å the centre of the molecule appears black, whereas at 2·9 Å it is white, *cf.* Fig. 2*c*), and is recognizable as such to a crystal thickness of 130 Å;

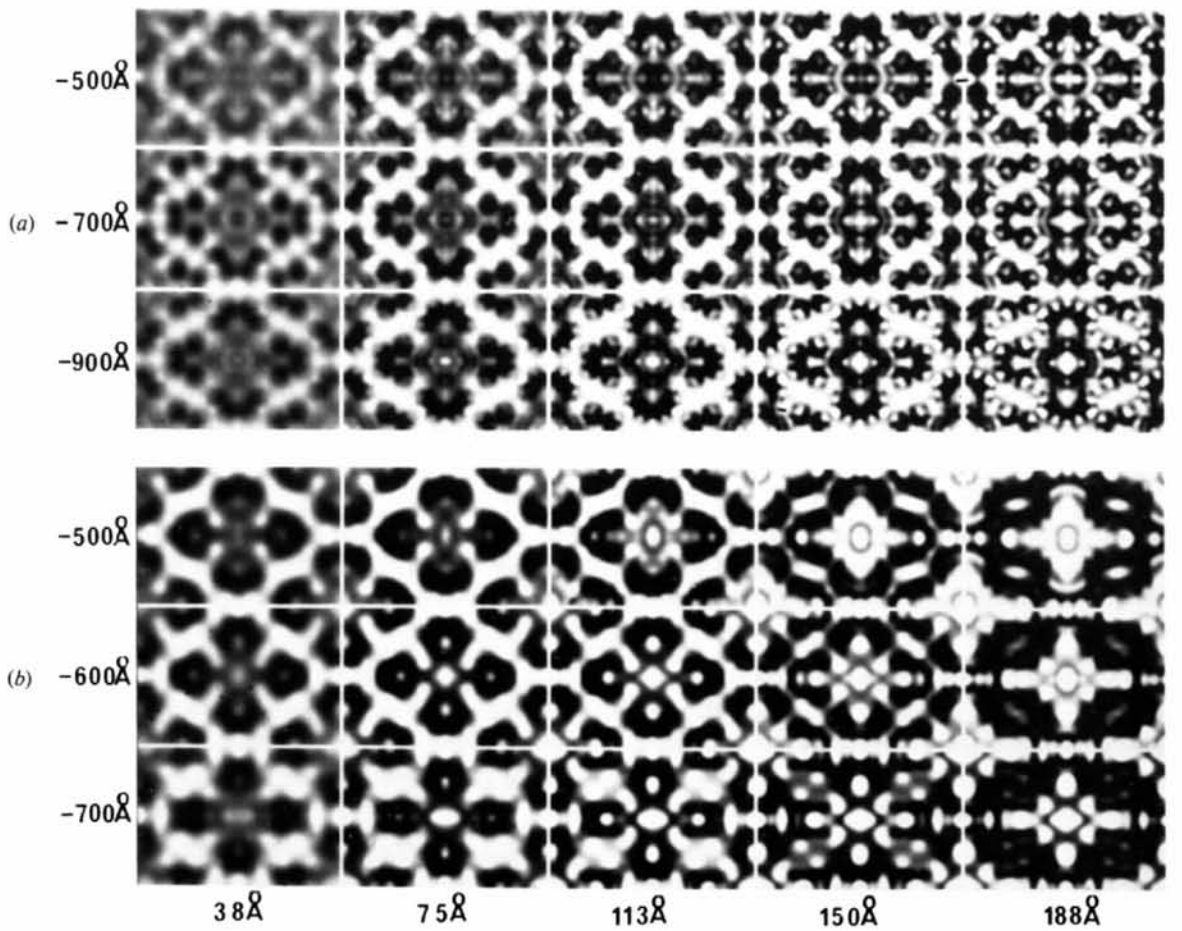

Fig. 6. Thickness-series comparisons of copper hexadecachlorophthalocyanine at electron energies of (*a*) 500 and (*b*) 100 keV at close to the Scherzer focus values: the 500 keV parameters are as for Fig. 3 whilst those used for 100 kV are $C_s = 0{\cdot}7$ mm, $\Delta = 100$ Å, $\alpha_i = 1{\cdot}0$ mrad.

above this value the image loses its identity, showing merely a white cross at the position of the molecule. This is quite a different mode of failure to that at 500 kV, and reflects the difference in the resolution-limiting factors of 100 kV electron microscopes and those of 500 kV and higher voltage.

In 100 kV microscopes the factor that limits resolution is incident-electron-beam convergence, a relatively high value (typically 1 mrad half-angle at the specimen) being necessary to produce a bright image on the viewing screen as well as reasonable exposure times. At higher voltages convergence is reduced (a typical value is 0·3 mrad) and the limiting factor becomes the spread of focus caused by a combination of relatively large chromatic aberration coefficient and high-voltage instabilities. In the linear-image (thin-crystal) domain, both convergence and spread of focus act rather like soft apertures on the amplitudes of diffracted beams contributing to the image (see *e.g.* Anstis & O'Keefe, 1976), thus limiting the overall linear-image resolution. In images from thicker crystals, second-order (or non-linear) interferences contribute significantly to the image, and it is sometimes assumed that these will be damped in the same manner as linear contributions. However, it can be shown (O'Keefe, 1979) that non-linear terms are strongly damped by convergence, but much less strongly by spread of focus (the '**g** minus **g**' term not at all). In the 500 kV images of Fig. 6(*a*), the linear (thin-crystal) image has a resolution of approximately 2·5 Å while the thicker-crystal image may be considered as a superposition of a linear image of this resolution and a second-order one formed from selected interferences between diffracted beams out to 1·8 Å (the limit set on non-linear contributions by a convergence of 0·3 mrad at Scherzer defocus). In the 100 kV images (Fig. 6*b*) both linear and non-linear contributions are formed from diffracted beams out to only 3 Å (the limit set by 1 mrad convergence). The second-order contribution to the 100 kV images is thus much less, so that the 'donut' effect of sharp white peak superposed onto blunt black ones is confined to the blacker areas of the horizontal arms of the molecular shape [in the Scherzer defocus (−600 Å) image for crystals thicker than 130 Å, and in the −500 Å image above 100 Å thickness]; the image fails with thickness owing to phase and amplitude changes in the diffracted beams rather than multiple interferences amongst these beams.

Discussion

The image simulations summarized here indicate several factors which are conducive to the high-resolution imaging of molecular crystals, despite their considerable susceptibility to electron-beam damage, and hence the necessity for using low-dose minimum exposure techniques. For example, simulated WPO images can be used for interpretation of experimental micrographs over a comparatively wide range of defocus (perhaps −400 to −1000 Å) and for crystals of moderate thickness (perhaps up to ~250 Å – although this value is focus dependent). This favourable situation has been shown to stem directly from the monotonic fall-off of the structure factors with increasing diffracted orders, as well as the primarily low-atomic-number components of these materials. It should be noted, however, that any improvement in resolution, perhaps resulting from the use of a liquid-helium specimen stage, which leads to the inclusion in the image of a higher-order structure factor of larger amplitude (such as beams corresponding to definition of individual aromatic rings) will result in a very restricted range of focus and thickness for a directly interpretable image (see O'Keefe *et al.*, 1982). In terms of the chemical information discussed previously this implies that image interpretation for specimens fulfilling the WPO criteria should be valid for both the perfect crystal and local imperfections with regard to molecular position. Likewise, for molecules with accentuated angularity, such as the phthalocyanines, the resolution of the approximate shape, and hence the molecular orientation, would also be valid. However, for details of internal ring structure and minor deviations from perfection – such as mono-substituted derivatives – the imaging criteria are much more stringent.

In our discussions of image interpretability we have simply considered the qualitative likeness between the WPO images and those simulated using the full multislice formulation, rather than formally introducing some sort of reliability factor as invoked by Jap & Glaeser (1980). However, a matrix of simulated images as a function both of thickness and defocus should still enable the interpretation of micrographs recorded under non-optimum conditions. The dangers of *ad hoc* interpretation of images obtained far from WPO conditions is well-illustrated by coronene images at −2000 Å defocus (Fig. 3); when viewed in isolation, these images suggest an array of white pointed molecular shapes aligned from lower left to top right of the field of view. It is also relevant here to point out a further conclusion of our simulations that, contrary to the imaging of metals, semiconductors and oxides, there appears to be no recurrence of images resembling the WPO image as a function of either thickness or defocus. Moreover, no significant gain in resolution is achieved by drastic under-focusing.

It is also of interest that because of the behaviour of contrast with defocus or thickness there is no danger of misinterpretation of molecular position over a relatively wide range of focus for this size of molecule. However, for smaller molecules, such as benzene and its derivatives, it is probable that molecular position could be mistaken unless the focus and thickness was within a much smaller range.

We are grateful to the Science and Engineering Research Council for financial support.

References

ANSTIS, G. R. & O'KEEFE, M. A. (1976) *Proc. 34th Ann. Meet. EMSA*, edited by G. W. BAILEY, pp. 480–481. Baton Rouge: Claitor.

DONALDSON, D. M. & ROBERTSON, J. M. (1954). *Proc. R. Soc. London Ser. A*, **220**, 157–170.

FRYER, J. R. (1979). *Acta Cryst.* A**35**, 327–332.

FRYER, J. R., CAMPS, R. A. & SMITH, D. J. (1982). *Electron Microscopy* 1982, Vol. 2, pp. 449–450. Frankfurt: Deutsche Gesellschaft für Elektronenmikroskopie e.V.

FRYER, J. R. & SMITH, D. J. (1982). *Proc. R. Soc. London Ser. A*, **381**, 225–240.

GOODMAN, P. & MOODIE, A. F. (1974). *Acta Cryst.* A**30**, 280–290.

International Tables for X-ray Crystallography (1974). Vol. IV. Birmingham: Kynoch Press.

JAP, B. & GLAESER, R. M. (1980). *Acta Cryst.* A**36**, 57–67.

KERR, K. A., ASHMORE, J. P. & SPEAKMAN, J. C. (1975). *Proc. R. Soc. London Ser. A*, **344**, 199–215.

KIRKLAND, E. J. (1982). *Ultramicroscopy*, **9**, 45–64.

LYNCH, D. F., MOODIE, A. F. & O'KEEFE, M. A. (1975). *Acta Cryst.* A**31**, 300–307.

MURATA, Y., FRYER, J. R. & BAIRD, T. (1977). *Acta Cryst.* A**33**, 198–200.

O'KEEFE, M. A. (1973). *Acta Cryst.* A**29**, 389–401.

O'KEEFE, M. A. (1979). *Proc. 37th Ann. Meet. EMSA*, edited by G. W. BAILEY, pp. 556–557. Baton Rouge: Claitor.

O'KEEFE, M. A. & BUSECK, P. R. (1979). *Trans. Am. Crystallogr. Assoc.* **15**, 27–46.

O'KEEFE, M. A., BUSECK, P. R. & IIJIMA, S. (1978). *Nature (London)*, **274**, 322–324.

O'KEEFE, M. A., FRYER, J. R. & SMITH, D. J. (1982). *Electron Microscopy and Analysis* 1981, edited by M. J. GORINGE, pp. 337–340. Bristol and London: Institute of Physics.

O'KEEFE, M. A. & PITT, A. J. (1980). *Electron Microscopy* 1980, Vol. 1. *Physics*, edited by P. BREDEROO & G. BOOM, pp. 122–123: Leiden: Seventh European Congress on Electron Microscopy Foundation.

PIROUZ, P. (1981). *Acta Cryst.* A**37**, 465–471.

ROBERTSON, J. M. & TROTTER, J. (1961). *J. Chem. Soc.* pp. 1280–1284.

ROBERTSON, J. M. & WHITE, J. G. (1945). *J. Chem. Soc.* pp. 607–617.

SAIJO, H., KOBAYASHI, T. & UYEDA, N. (1977). *J. Cryst. Growth.* **40**, 118–124.

SCHMIDT, G. M. J. (1971). *Pure Appl. Chem.* **27**, 647–678.

SELF, P. G., O'KEEFE, M. A., BUSECK, P. R. & SPARGO, A. E. C. (1983). *Ultramicroscopy*. In the press.

SMITH, D. J. (1980). *Electron Microscopy* 1980, Vol. 4. *High Voltage*, edited by J. VAN LANDUYT & G. BOOM, pp. 122–129. Leiden: Seventh European Congress on Electron Microscopy Foundation.

SMITH, D. J., CAMPS, R. A., FREEMAN, L. A., HILL, R., NIXON, W. C. & SMITH, K. C. A. (1983). *J. Microsc.* **130**, 127–136.

SMITH, D. J. & FRYER, J. R. (1981). *Nature (London)*, **291**, 481–482.

SMITH, D. J. & O'KEEFE, M. A. (1983). *Acta Cryst.* A**39**, 139–148.

UNWIN, P. N. T. & HENDERSON, R. (1975). *J. Mol. Biol.* **94**, 425–440.

UYEDA, N. & ISHIZUKA, K. (1974). *J. Electron Microsc.* **23**, 79–88.

VEBLEN, D. R. & BUSECK, P. R. (1980). *Am. Mineral.* **65**, 599–632.

Acta Cryst. (1983). A**39**, 847–853

Moments of the Probability Density Function of R_2 Approached *Via* Conditional Probabilities. III. Models Containing Correctly as well as Incorrectly Placed Atoms in the Space Groups $P1$ and $P\bar{1}$

BY W. K. L. VAN HAVERE AND A. T. H. LENSTRA

University of Antwerp (UIA), Department of Chemistry, Universiteitsplein 1, B-2610 Wilrijk, Belgium

(*Received* 3 *June* 1982: *accepted* 13 *May* 1983)

Abstract

First and second moments of $P(R_2)$ are evaluated for models containing correctly as well as incorrectly placed atoms, denoted symbolically by $\{g, f\}$. Formulas are derived, valid for the space groups $P1$ and $P\bar{1}$, using explicitly the set of observed reflections. Extrapolation through the introduction of an *averaged* structure allows some general conclusions to be drawn concerning possible strategies used in automated structure determinations. A select elimination of data points from the R_2 check on the correctness of an atomic position severely limits the usefulness of the R_2 criterion. A check based on R_2^n has no better characteristics than one based on R_2. An R_2 criterion together with a zero-atom strategy has better chances of being successful than a random-atom approach.

0108-7673/83/060847-07$01.50

1. Introduction

In automated crystal-structure determination one needs to discriminate between correct and incorrect models related to the observed structure. The models to be tested can come out of any traditional solution procedure. In order to describe the various situations